Coherent lensless diffraction imaging via multicore fiber for label-efficient microplastics characteristic discrimination

Yunfei Tian, Rongzhou Chen, Yanmin Zhu, Jingyan Chen, and Edmund Y. Lam*

Department of Electrical and Electronic Engineering, The University of Hong Kong, Pokfulam, Hong Kong SAR, China

ABSTRACT

The widespread exposure of microplastics (MPs) to environmental and biological systems makes the rapid identification of their damage status a critical task. This deformation influences how MPs migrate, degrade, and interact with organisms, thereby shaping their environmental fate and ecological risk. However, traditional bright-field microscopy suffers from degraded performance under defocused and low-contrast conditions, and benchtop systems are also difficult to deploy in situ in confined spaces. To address these challenges, we propose a lightweight method combining multicore fiber bundle-based coherent defocused imaging with self-supervised representation learning. When only an extremely small number of annotations are provided, semi-supervised constraints, including weighted updates and soft penalties are introduced to enhance cluster-class alignment. This scheme eliminates the need for holographic reconstruction and features a thin, flexible probe, making it suitable for in-situ and online detection in confined environments. The results demonstrate that combining physically enhanced coherent imaging with self-supervised features enables robust differentiation between damaged and undamaged MPs at low annotation cost, and provides a feasible path for on-site deployment.

Keywords: Microplastics, multicore fiber, coherent defocused imaging, self-supervised representation learning

1. INTRODUCTION

Microplastics (MPs) are ubiquitous in seawater, freshwater, sediments, soils, and biota, and their damaged or intact states are closely related to environmental behavior and ecological risk.[1] Rapid and objective differentiation between damaged and undamaged MPs can support source tracing, risk assessment, and the formulation of mitigation and monitoring strategies. However, in-situ detection faces multiple challenges such as low imaging contrast, strong vibration and medium disturbance, and limited spatial accessibility.[2] Conventional bright-field microscopy suffers a pronounced decline in recognition performance under conditions of small refractive-index contrast, narrow depth of field, defocus, and background stray light.[3] Manual interpretation is further constrained by strong subjectivity and poor reproducibility. Meanwhile, benchtop microscopic systems are bulky, require precise focusing, and are difficult to deploy for in-situ monitoring in confined spaces such as pipelines and cavities.[4]

Digital holographic microscopy offers high throughput and phase sensitivity for particle analysis.[5,6] A single intensity hologram allows numerical back-propagation to recover complex amplitude and phase, thereby characterizing morphology, refractive index, and three-dimensional position, and enabling simultaneous capture of multiple particles within a large depth of field. Nevertheless, its stringent requirements on interference stability, heavy dependence on system calibration and numerical reconstruction, and high complexity of both instrumentation and algorithms hinder stable deployment in confined environments.[7] Deep-learning methods have also been applied to MPs recognition, but they typically require large amounts of annotated data and sharply focused images, and exhibit limited robustness to cross-domain changes (illumination or imaging conditions) and field deployment.[8,9]

To address volume and accessibility constraints, multicore optical fibers have been employed for lensless imaging and holographic micro-endoscopy.[10] Fiber-bundle imaging combined with computational reconstruction or scanning can alleviate honeycomb sampling and resolution limitations, and the fiber probe itself provides

Send correspondence to Edmund Y. Lam: elam@eee.hku.hk

Holography, Diffractive Optics, and Applications XV, edited by Changhe Zhou, Ting-Chung Poon, Liangcai Cao, Hiroshi Yoshikawa, Proc. of SPIE Vol. 13719, 137191L
2025 Published by SPIE · 0277-786X · doi: 10.1117/12.3073960

engineering advantages such as small diameter, flexibility, and disposability.[11,12] However, prior work has mainly focused on live micro-endoscopy and tissue imaging, where system performance remains strongly dependent on probe stability, calibration accuracy, and reconstruction algorithms.[13]

We propose and experimentally validates a MPs damage-state recognition method that integrates coherent multicore fiber imaging with self-supervised representation learning. On the imaging side, coherent defocused images of MPs are acquired by laser illumination and multicore fiber transmission. On the algorithmic side, global representations are extracted by a frozen DINOv2 backbone [14] and clustered using unsupervised k-means,[15] with optional semi-supervised guidance from a very small number of labeled samples, thus avoiding end-to-end training.[16] Experimental results demonstrate that combining physics-enhanced coherent imaging with self-supervised representation enables robust identification of mechanical damage in MPs under spatial and annotation constraints, and shows strong potential for in-situ and endoscopic environmental monitoring.

2. METHOD

2.1 Experimental Setup

We constructed a fiber-bundle–based transmission system for coherent imaging, similar to the coaxial holographic system.[17,18] Fig. 1(a) illustrates the optical layout. A 650 nm laser is spatially filtered and collimated to illuminate the specimen. The transmitted field propagates in free space and is coupled into the distal facet of a 600 µm multicore fiber bundle; at the proximal side, the bundle end-face is imaged onto a CMOS camera through a microscope objective (40X), yielding a coherent defocus shadowgraph dominated by diffraction and speckle contrast. Fig. 1(b) shows a 100 µm polystyrene MP under conventional bright-field microscopy for reference; Fig. 1(c) records the fiber-bundle end-face with no specimen to verify the imaging geometry and focal plane; Fig. 1(d) presents the coherent defocus image produced by our setup under laser illumination.

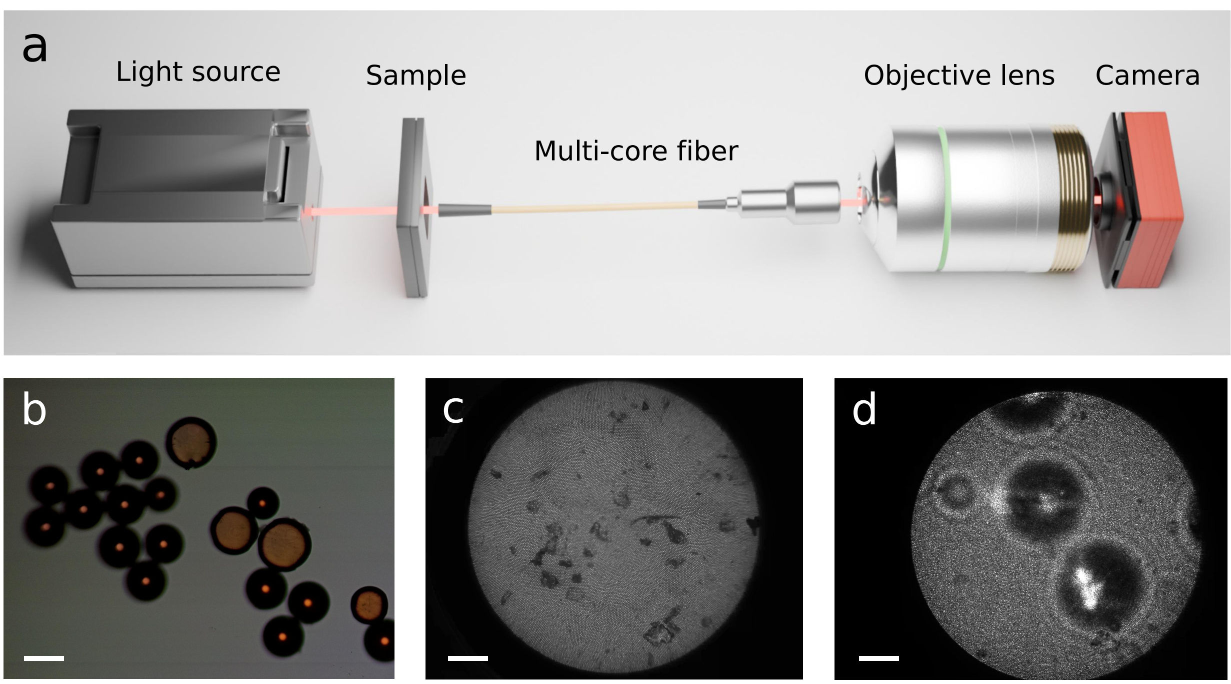

Figure 1. **Optical principle and image formation.** (a) Schematic of the coherent, fiber-bundle–based transmission setup (red laser; 600 µm multicore fiber; camera). (b) Bright-field microscope image of an intact 100 μm polystyrene microplastic bead. (c) Raw camera view of the fiber-bundle end-face with no specimen. (d) Coherent defocus shadowgraph produced by the proposed system under laser illumination. The scale bar in (b-d) represents 100 μm.

For reproducibility, the specimen-to-fiber distance is adjusted on a three-axis stage, and a small axial offset Δz is introduced to convert phase variations into intensity contrast in a controlled manner. Two specimen classes are acquired: intact MPs (as-received, spherical or near-spherical) and mechanically damaged MPs (mildly crushed, exhibiting cracks, dents, or deformation). Samples are placed on a transparent substrate and translated laterally to collect multiple fields of view; camera exposure and gain are held constant within each condition to avoid saturation. For comparison, we also acquire data with a broadband LED as an incoherent illuminant under the same geometry.

2.2 Algorithm Design

We adopt a frozen representations with lightweight clustering pipeline: each image is embedded by a pretrained DINOv2 encoder and then classified via k-Means in the embedding space. When a handful of labels are available, we enable simple semi-supervised constraints to improve cluster–class alignment. The t-SNE plots are used for 2D visualization only and do not affect training or clustering.

Feature extraction and preprocessing involves resizing and cropping inputs to 518×518 and normalized with ImageNet statistics. We use DINOv2 ViT-S/14 to obtain an embedding $f_i \in \mathbb{R}^D$ for the i-th image.[14] We apply Z-score normalization

$$x_i = \frac{f_i - \mu}{\sigma}, \tag{1}$$

where $\mu \in \mathbb{R}^D$ and $\sigma \in \mathbb{R}^D$ are the per-dimension mean and standard deviation over the dataset, and x_i is the standardized feature. We then perform ℓ_2 normalization $\tilde{x}_i = \frac{x_i}{\|x_i\|_2}$ to place features on the unit sphere, which makes Euclidean distance consistent with cosine similarity for spherical k-Means.

For unsupervised k-Means,[15] with $k = 2$ clusters, we solve

$$\min_{\{y_i\},\,\{c_k\}} \sum_{i=1}^{N} \left\|\tilde{x}_i - c_{y_i}\right\|_2^2, \tag{2}$$

where $y_i \in \{0, 1\}$ is the cluster label of sample i, $c_k \in \mathbb{R}^D$ is the centroid of cluster k, and $\|\cdot\|_2$ denotes the Euclidean norm. We use k-Means++ initialization with $n_{\text{init}} = 20$ restarts and select the most stable solution across restarts.[19] Random seeds and filename ordering are fixed to avoid order bias.

For semi-supervised clustering (few labels),[16] let $\mathcal{S} \subset \{1, \ldots, N\}$ be a small labeled set with class labels $\ell_i \in \{0, 1\}$ (we take 0 = Damaged and 1 = Intact). We employ two lightweight mechanisms.

Weighted centroid updates:

$$c_k = \frac{\sum\limits_{i \in \{\, j \mid y_j = k \,\}} w_i \, \tilde{x}_i}{\sum\limits_{i \in \{\, j \mid y_j = k \,\}} w_i}. \tag{3}$$

$$w_i \;=\; \begin{cases} w_{\text{sup}} & \text{if } i \in \mathcal{S}, \\ 1 & \text{otherwise.} \end{cases} \tag{4}$$

Soft penalty for wrong clusters:

$$d^2(i,k) \;\leftarrow\; \|\tilde{x}_i - c_k\|_2^2 \;+\; \alpha\, \mathbf{1}[\, k \neq \ell_i \,], \tag{5}$$

where $d^2(i,k)$ denotes the squared distance from sample i to centroid c_k, $\alpha > 0$ is a penalty coefficient, and $\mathbf{1}[\cdot]$ is the indicator function that equals 1 if the condition holds and 0 otherwise.

These mechanisms gently steer the iterations toward label-consistent partitions without hard assignments; if one class has no labels, initialization still proceeds via k-Means++.

We use ground-truth labels $y_i^{\text{true}} \in \{0, 1\}$ for cluster–class mapping and evaluation. After clustering, cluster IDs $\{0, 1\}$ are mapped to the semantic classes $\{$Damaged(0), Intact(1)$\}$ via majority voting or Hungarian matching to maximize accuracy. We report four evaluation outputs in a single pipeline: the confusion matrix for Damaged versus Intact, a two-dimensional t-SNE visualization of the embeddings, the precision–recall (PR) curve, and the ROC curve. For PR and ROC we require a continuous score per sample. Let k_{pos} be the cluster mapped to the positive class (Damaged) and k_{neg} be the cluster mapped to the negative class (Intact).[20] With squared distances

$$d^2(i,k) \;=\; \|\tilde{x}_i - c_k\|_2^2, \tag{6}$$

we define the sample score

$$s_i \;=\; d^2\big(i,k_{\text{neg}}\big) \;-\; d^2\big(i,k_{\text{pos}}\big), \tag{7}$$

so that larger s_i indicates that sample i is closer to the positive centroid and thus more likely to be Damaged. The pairs $\{(y_i^{\text{true}}, s_i)\}_{i=1}^{N}$ are then used to compute the PR and ROC curves and their corresponding AUCs.

3. RESULTS AND DISCUSSION

3.1 Classification Results and Analysis

As illustrated in Fig. 2, we show representative coherent-defocus intensity images acquired with the same configuration (650 nm laser illumination and fiber-bundle imaging). The top row contains mechanically damaged MPs; the bottom row contains intact ones. Each column corresponds to a different specimen or field of view.

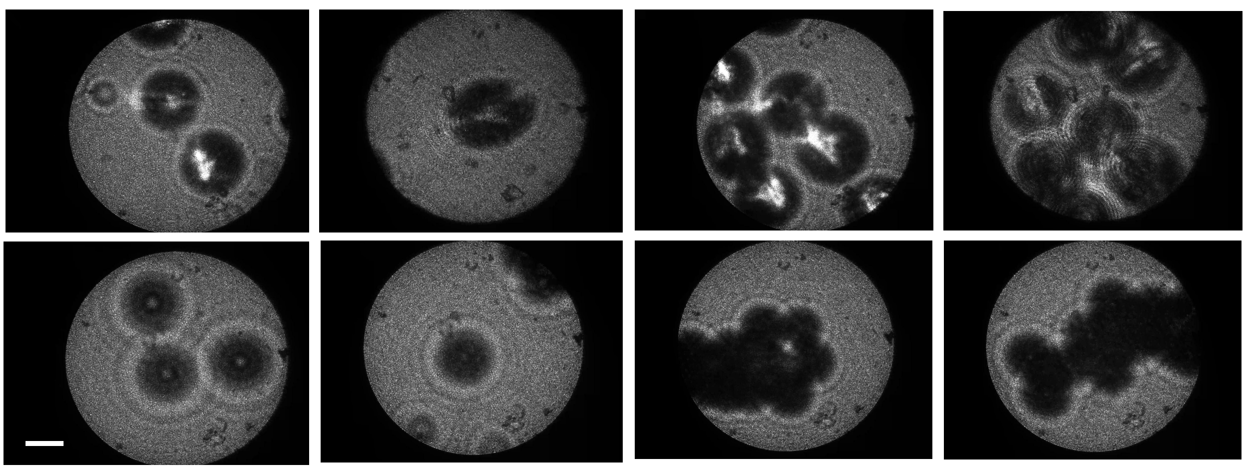

Figure 2. **Representative examples acquired by the system.** Top row: mechanically damaged microplastics; Bottom row: intact microplastics. Each pane shows a different specimen or field of view under the same coherent-defocus imaging configuration. The scale bar represents 100 μm.

Damaged particles typically present irregular, asymmetric dark silhouettes accompanied by bright lobes and stronger speckle modulation, reflecting surface cracks, dents, or deformations. In contrast, intact particles exhibit smoother, near-concentric shadow patterns with weaker internal hot spots. These appearance differences are consistent across specimens and motivate the use of feature-based clustering for classification.

Fig. 3 summarizes the learning-based analysis using frozen DINOv2 embeddings and k-Means. The top row corresponds to the purely unsupervised setting, whereas the bottom row uses only ten labeled seeds to guide a semi-supervised variant. In Fig. 3(a), the confusion matrices show that unsupervised clustering already recovers most Damaged samples but confuses a sizable portion of Intact ones (66.6% correct; 33.4% misclassified). Injecting ten labels eliminates these Intact errors (100.0% correct) and maintains a high recall for Damaged (87.3%), indicating a clear improvement in cluster–class alignment.

Fig. 3(b) visualizes the same DINOv2 feature space with t-SNE, colored by predicted classes. The semi-supervised result reduces mixing near the decision boundary and yields more coherent class-consistent islands. Fig. 3(c) and (d) quantify the effect using distance-based continuous scores: the average precision increases from

0.918 (unsupervised) to 0.997 (semi-supervised), and the ROC AUC rises from 0.846 to 0.994. Overall, a handful of labels is sufficient to stabilize the boundary around Intact samples while preserving the sensitivity to Damaged ones, validating the effectiveness of lightweight semi-supervision on top of frozen self-supervised representations.

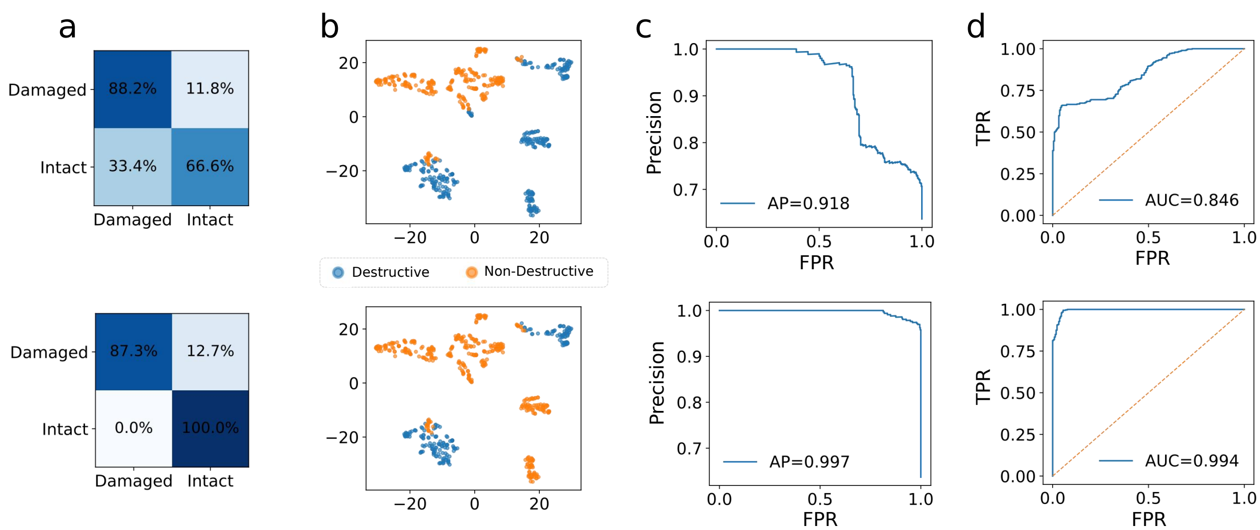

Figure 3. **Learning-based classification with DINOv2 features and k-Means.** Top row: unsupervised k-Means applied to frozen DINOv2 features. Bottom row: semi-supervised k-Means with 10 labels. Within each row: (a) confusion matrix for Damaged vs Intact; (b) t-SNE visualization; (c) precision–recall (PR) curve; (d) ROC curve.

3.2 Coherent and Incoherent Illumination Imaging

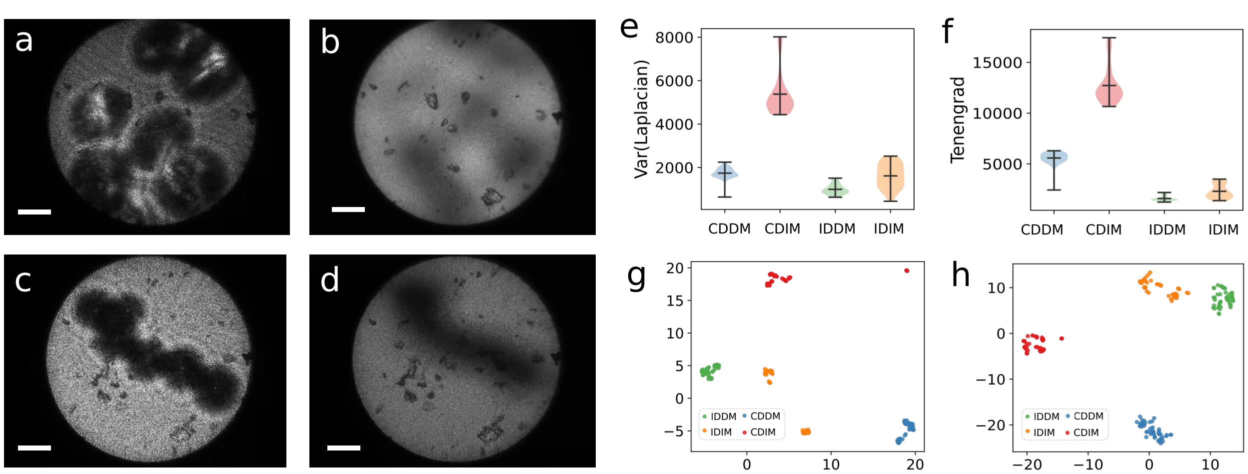

Figure 4. **Coherent vs. incoherent illumination under defocus.** (a) Coherent-Defocus (laser) Damaged Microplastics (CDDM); (b) Incoherent-Defocus (led) Damaged Microplastics (IDDM); (c) Coherent-Defocus Intact Microplastics (CDIM); (d) Incoherent-Defocus Intact Microplastics (IDIM). Panels (e–h) summarize statistics over N=48 images per condition: (e) Var(Laplacian) sharpness (violin plots); (f) Tenengrad sharpness (violin plots); (g) UMAP of DINOv2 features (four classes in one plot); (h) t-SNE of DINOv2 features. Coherent illumination preserves discriminative high-frequency content and yields markedly better separability than incoherent (defocused) illumination. The scale bar in (a-d) represents 100 μm.

Fig. 4 contrasts coherent and incoherent illumination under defocus across two specimen states. Fig. 4(a–d) show typical raw intensity frames: with laser illumination, both Damaged (a) and Intact (c) particles exhibit pronounced diffraction- and speckle-driven contrast; with LED illumination, Damaged (b) and Intact (d) appear low-pass filtered with weakened internal texture and reduced edge definition. Fig. 4(e) and (f) aggregate N=48 images per condition using Var(Laplacian) and Tenengrad, respectively. The coherent conditions yield markedly higher sharpness: Coherent-Defocus Intact Microplastics (CDIM) attains the highest scores, Coherent-Defocus Damaged Microplastics (CDDM) ranks second, whereas Incoherent-Defocus Damaged Microplastics (IDDM) and Incoherent-Defocus Intact Microplastics (IDIM) cluster at substantially lower values, indicating a compressed high-frequency content under incoherent illumination. Fig. 4 (g) and (h) visualize DINOv2 embeddings with UMAP and t-SNE. The four conditions form well-separated groups, and the coherent cases exhibit tighter intra-class compactness and larger inter-class gaps, consistent with the sharpness statistics. Overall, coherent-defocus imaging preserves discriminative spatial frequencies and leads to superior separability compared with incoherent illumination.

4. CONCLUSION

This paper proposes a MPs damage status assessment scheme for confined scenarios, which integrates coherent defocused imaging based on a multicore fiber bundle, frozen self-supervised representations, and lightweight clustering. The experimental system adopts a 650 nm wavelength laser for illumination and a multicore fiber bundle with a diameter of 600 µm. Without the need for holographic image reconstruction, it directly acquires coherent defocused intensity patterns that are highly sensitive to morphological deformation. On the algorithm side, DINOv2 is used to extract stable features, and k-Means is performed in the representation space, achieving effective separation in the unsupervised setting. A small number of annotations (e.g., 10 images) further align clusters with semantic categories through soft constraints. Control experiments of the system show that the coherent defocused condition can preserve discriminative mid-to-high frequency information. A continuous scoring function constructed based on cluster-class centroid distance significantly improves the PR/ROC metrics under the semi-supervised setting, verifying the effectiveness and scalability of the "physically enhanced imaging and self-supervised features" framework. This provides a portable and low-annotation-cost path for rapid MPs assessment in real-world scenarios. The scheme has engineering advantages such as a thin and flexible probe, long-distance light field transmission, compact structure, and low cost, and has potential application value in in-situ monitoring of confined spaces such as pipelines and cavities.

5. ACKNOWLEDGMENT

The work is supported by the Research Grants Council of Hong Kong (GRF 17201822 and RIF R7003-21).

REFERENCES

[1] De Souza Machado, A. A., Kloas, W., Zarfl, C., Hempel, S., and Rillig, M. C., "Microplastics as an emerging threat to terrestrial ecosystems," *Global Change Biology* **24**(4), 1405–1416 (2018).

[2] Zhu, Y., Li, Y., Huang, J., Zhang, Y., Ho, Y.-W., Fang, J. K.-H., and Lam, E. Y., "Advanced optical imaging technologies for microplastics identification: Progress and challenges," *Advanced Photonics Research* **5**(11), 2400038 (2024).

[3] Nigamatzyanova, L. and Fakhrullin, R., "Dark-field hyperspectral microscopy for label-free microplastics and nanoplastics detection and identification in vivo: A caenorhabditis elegans study," *Environmental Pollution* **271**, 116337 (2021).

[4] Zhu, Y., Li, Y., Huang, J., Zhang, Y., and Lam, E. Y., "Holographic and polarization features analysis for microplastics characterization and water monitoring," in [*Multimodal Sensing and Artificial Intelligence: Technologies and Applications III*], **12621**, 234–236, SPIE (2023).

[5] Huang, J., Zhu, S., Li, Y., Wang, C., and Lam, E. Y., "Computational polarized holography for automatic monitoring of microplastics in scattering aquatic environments," *APL Photonics* **10**(3) (2025).

[6] Zhu, Y., Li, Y., Huang, J., and Lam, E. Y., "Smart polarization and spectroscopic holography for real-time microplastics identification," *Communications Engineering* **3**(1), 32 (2024).

[7] Zhang, Y. and Lam, E. Y., "Robust holographic imaging for real-world applications with joint optimization," *Optics Express* **33**(3), 5932–5944 (2025).

[8] Zhu, Y., Hang Yeung, C., and Lam, E. Y., "Digital holographic imaging and classification of microplastics using deep transfer learning," *Applied Optics* **60**(4), A38–A47 (2020).

[9] Zhu, Y., Yeung, C. H., and Lam, E. Y., "Digital holographic microplastics detection and characterization in heterogeneous samples via deep learning," in [*Twelfth International Conference on Information Optics and Photonics*], **12057**, 789–794, SPIE (2021).

[10] Badt, N. and Katz, O., "Real-time holographic lensless micro-endoscopy through flexible fibers via fiber bundle distal holography," *Nature Communications* **13**(1), 6055 (2022).

[11] Feng, H., Chen, X., Zhu, R., Xiong, Y., Chen, Y., Lu, Y., and Xu, F., "Seeing at a distance with multicore fibers," *Opto-Electronic Advances* **7**(7), 230202–1 (2024).

[12] Feng, H., Zhu, R., and Xu, F., "Feature-enhanced fiber bundle imaging based on light field acquisition," *Advanced Imaging* **1**(1), 011002 (2024).

[13] Kang, M., Choi, W., Hong, J. H., Katz, O., Lee, B., Kim, G. H., Choi, Y., and Choi, W., "Flexible-type ultrathin holographic endoscope for microscopic imaging of unstained biological tissues," in [*Imaging Systems and Applications*], ITu4E–3, Optica Publishing Group (2022).

[14] Oquab, M., Darcet, T., Moutakanni, T., Vo, H., Szafraniec, M., Khalidov, V., Fernandez, P., Haziza, D., Massa, F., El-Nouby, A., et al., "Dinov2: Learning robust visual features without supervision," *arXiv preprint arXiv:2304.07193* (2023).

[15] Sinaga, K. P. and Yang, M.-S., "Unsupervised K-means clustering algorithm," *IEEE Access* **8**, 80716–80727 (2020).

[16] Lin, F. and Cohen, W. W., "Semi-supervised classification of network data using very few labels," in [*2010 international conference on advances in social networks analysis and mining*], 192–199, IEEE (2010).

[17] Li, Y., Zhu, Y., Huang, J., Ho, Y.-W., Fang, J. K.-H., and Lam, E. Y., "High-throughput microplastic assessment using polarization holographic imaging," *Scientific Reports* **14**(1), 2355 (2024).

[18] Zhu, Y., Yeung, C. H., and Lam, E. Y., "Microplastic pollution monitoring with holographic classification and deep learning," *Journal of Physics: Photonics* **3**(2), 024013 (2021).

[19] Arthur, D. and Vassilvitskii, S., "k-means++: The advantages of careful seeding," tech. rep., Stanford (2006).

[20] Jaskowiak, P. A., Costa, I. G., and Campello, R. J., "The area under the roc curve as a measure of clustering quality," *Data Mining and Knowledge Discovery* **36**(3), 1219–1245 (2022).